The nanoscale organization of the Nipah virus fusion protein informs new membrane fusion mechanisms.

Qian Wang[1], Jinxin Liu[1], Yuhang Luo[1], Vicky Kliemke[1], Giuliana Leonarda Matta[1], Jingjing Wang[1], Qian Liu[1,2,*]

[1] Institute of Parasitology, Faculty of Agricultural and Environmental Sciences, McGill University, Saint Anne de Bellevue, Canada.

[2] McGill Center for Viral Diseases, Lady Davis Institute, Montreal, Canada.

Abstract.

Paramyxovirus membrane fusion requires an attachment protein for receptor binding and a fusion protein for membrane fusion triggering. Nipah virus (NiV) attachment protein (G) binds to ephrinB2 or -B3 receptors, and fusion protein (F) mediates membrane fusion. NiV-F is a class I fusion protein and is activated by endosomal cleavage. The crystal structure of a soluble GCN4-decorated NiV-F shows a hexamer-of-trimer assembly. Here, we used single-molecule localization microscopy to quantify the NiV-F distribution and organization on cell and virus-like-particle membranes at a nanometer resolution. We found that NiV-F on biological membranes forms distinctive clusters that are independent of endosomal cleavage or expression levels. The sequestration of NiV-F into dense clusters favors membrane fusion triggering. The nano-distribution and organization of NiV-F are susceptible to mutations at the hexamer-of-trimer interface, and the putative oligomerization motif on the transmembrane domain. We also show that NiV-F nanoclusters are maintained by NiV-F-AP-2 interactions and the clathrin coat assembly. We propose that the organization of NiV-F into nanoclusters facilitates membrane fusion triggering by a mixed population of NiV-F molecules with varied degrees of cleavage and opportunities for interacting with the NiV-G/receptor complex. These observations provide insights into the in-situ organization and activation mechanisms of the NiV fusion machinery.

Introduction.

The family of *Paramyxoviridae* contains many clinically important viruses, such as human parainfluenza virus 1-3, measles virus, and Nipah virus (NiV). Paramyxoviruses code for two glycoproteins on the viral membranes for virus-cell membrane fusion. The receptor-binding proteins (RBP, HN/H/G) engage the host receptors and activate the refolding of the fusion protein (F) that merges the virus and cell membranes[1]. Paramyxovirus-F is a class I fusion protein, along with human immunodeficiency virus (HIV) envelope, influenza virus hemagglutinin, and severe acute respiratory syndrome coronavirus-2 (SARS-CoV-2) spike[1]. Paramyxovirus-F is a trimeric transmembrane protein with a “tree-like” structure at its prefusion conformation. Upon triggering by the RBP/receptor complex, paramyxovirus-F mediates fusion by inserting its N-terminal fusion peptides into the target membrane and undergoes a conformational change from pre- to post-fusion conformations, similarly to other class I fusion proteins. The refolding of the paramyxovirus-F overcomes the energy barrier for membrane fusion and leads to virus-cell and cell-cell membrane fusion.

NiV is a well-studied paramyxovirus due to its capability of human-human and human-animal transmissions, high mortality and morbidity rates, and the unavailability of vaccines or therapeutics for human use[2,3]. NiV is closely related to Hendra virus, Cedar virus, and the newly identified Langya virus[4]. NiV-F is expressed on the cell surface as an fusion-inactive form,

activated in the endosome by cathepsin B and L cleavage, and exocytosed to the cell surface as a fusion-active form[5,6]. NiV-G binds to ephrinB2 and/or -B3 receptors in host cells and triggers the refolding of F that leads to virus-cell membrane fusion[7]. Three complementary models of the NiV fusion activation mechanism have been proposed in the past. *In the first model*, the NiV-G and F form a complex before receptor engagement. The F/G interaction maintains F at a prefusion conformation. The receptor binding to G induces conformational changes in G, leading to the release and refolding of F. This model is supported by co-immunoprecipitation and conformational antibody binding assays[8,9]. *In the second model*, NiV-F exists as hexamer-of-trimers, and the fusion peptides are sequestered at the hexameric interface. The activation of one single trimer by the NiV-G/ephrinB2 complex can be transmitted to all six trimers via the interfaces of the hexamer-of-trimers, leading to efficient F-triggering and fusion pore formation. This model is supported by the crystal structure of a GCN4-decorated NiV-F ectodomain and mutagenesis analysis of key amino acid residues at the hexameric interfaces[10]. *In a third model*, NiV-F and G do not form a complex before receptor binding. The NiV-G/ephrinB2 engagement clusters ephrinB2 and triggers F. F triggering leads to reduced mobility of a portion of F molecules that potentially contributes to fusion pore formation. This model is supported by the nanoscale distribution of NiV-F and G on cell membranes resolved by super-resolution microscopy and a single-particle tracking assay of NiV fusion protein at the interface between supported lipid bilayer and live cell membranes[11,12]. Although these models explain the NiV membrane fusion mechanisms from different perspectives, a link between the molecular structure and the fusion machinery on biological membranes remains unclear.

We attempted to address this link by analyzing the nano-organization of NiV-F at the prefusion state on biological membranes using single-molecule localization microscopy (SMLM) and mutagenesis analyses. We have shown that NiV-F forms clusters on biological membranes that are isolated from NiV-G[11]. Here, we show that NiV-F forms regular-sized nanoclusters on cell membranes regardless of the expression level or endosomal cleavage. The estimated size of NiV-F clusters on cell membrane is similar to that of the hexamer-of-trimer assemblies formed by the GCN4-decorated soluble NiV-F. The NiV-F nano-organization is altered by mutations at the hexameric interface and the putative oligomerization motifs at the transmembrane domain. NiV-F molecules enriched in nanoclusters favor membrane fusion activation. The NiV-F nanoclusters are stabilized by the interactions between NiV-F, the endocytosis adaptor complex AP-2, and the clathrin coat at the cell membranes. In summary, our study reveals the NiV-F nano-organization on the biological membranes and provides novel insights to the NiV fusion machinery *in situ*.

NiV-F forms regular-sized clusters that are not affected by the surface expression level.

We recently published that NiV-F formed distinctive nanoclusters on the plasma membrane regardless of the presence of NiV-G or ephrinB2[11]. To investigate the determinants of the NiV-F nano-organization, we used SMLM to probe the NiV-F at various conditions. SMLM generates super-resolution images with nanometer resolution by localizing blinks from individual fluorophores with a distance greater than the diffraction limit of light[13]. PK13 cells have a flat morphology that is suitable for SMLM imaging. PK13 cells express little endogenous ephrinB2 and -B3 receptors for NiV and thus can eliminate any potential receptor-dependent clustering. Cell surface NiV-F was detected using a FLAG tag in its extracellular domain[11]. The FLAG tags were employed to detect NiV-F because of the availability of high affinity and specificity anti-FLAG antibodies for a high labeling density, which is vital for the reconstruction accuracy of

SMLM images[14]. To rule out the effect of the FLAG tag on NiV-F clustering, we compared NiV-F clusters formed by NiV-F-FLAG to that of a NiV-F-HA construct. Both HA and FLAG tags were inserted after amino acid residue 104, right before the fusion peptide (Fig. S1A). Visual examination of the SMLM images reveals that NiV-F-FLAG and NiV-F-HA form similar clusters (Fig. S1B). The clustering tendency, indicated by Hopkins' index, is comparable between NiV-F-HA and NiV-F-FLAG (Fig. S1C), suggesting that NiV-F clustering is not affected by specific epitope tags.

Next, we investigated whether the nano-organization of NiV-F depends on the cell surface expression levels. The total cell surface expression level (CSE) of NiV-F in a selected cell was measured before the cell was subjected to SMLM imaging. The SMLM images show that NiV-F forms similar nanoclusters in both high-expression and low-expression cells (Fig. 1A and B). Our data show that the clustering tendency of NiV-F is independent of its CSE in individual cells (Fig. 1C). To gain a quantitative understanding of NiV-F nanoscale organization, we used a cluster identification method DBSCAN (Density-Based Spatial Clustering of Applications with Noise) that links the closely situated localizations in a propagative manner. We created cluster and density maps using Clus-DoC for representative high-expression and low-expression cells (Fig. 1D and E)[15]. Our data show that the estimated diameter of the NiV-F clusters ranges from 20-34 nm, with a peak at 24 nm (Fig. 1F). Nonetheless, the precise values of the cluster diameter are indicative rather than definite in SMLM as it could be affected by the labeling complex and the blinking property of the fluorophore. The distribution of the cluster diameter shows that ~60% of NiV-F clusters have similar sizes, indicating that NiV-F clusters maintain a quite uniform appearance. Interestingly, we noticed that the size of the clusters (Fig. 1G) and localization density (Fig. 1H) in clusters were similar between high- and low-expression cells, suggesting that the NiV-F organization in nanoclusters is not affected by the expression levels. Moreover, our data show that the high-expression cells have more clusters than the low-expression cells (Fig. 1I). These results suggest that changes in CSE may affect the number of NiV-F clusters on the plasma membrane (Fig. 1I), but not the clustering tendency of NiV-F (Fig. 1C), the size of the clusters (Fig. 1G), or the localization density within clusters (Fig. 1H). These data imply that the distribution and nano-organization of NiV-F are tightly regulated and may be important for membrane fusion activation. We also analyzed NiV-F distribution in different cell lines. HeLa cells express ephrinB2 and -B3, and thus are NiV permissive cells. The overall NiV-F nano-organization seems quite similar on PK13 and HeLa cells, agreeing with our previous results (Fig. S2A)[11]. The Hopkins' indices are also similar for NiV-F on PK13 and HeLa cells (Fig. S2B). The DBSCAN analysis shows that the percentage localizations in clusters (Fig. S2C), the relative density defined as the ratio of the localization density in clusters to the total localization density in the selected region (Fig. S2D), and cluster diameters (Fig. S2E) are comparable for NiV-F on PK13 and HeLa cells. These results suggest that NiV-F clusters are minimally affected by the cell lines of expression or the presence of the ephrinB2 and/or -B3.

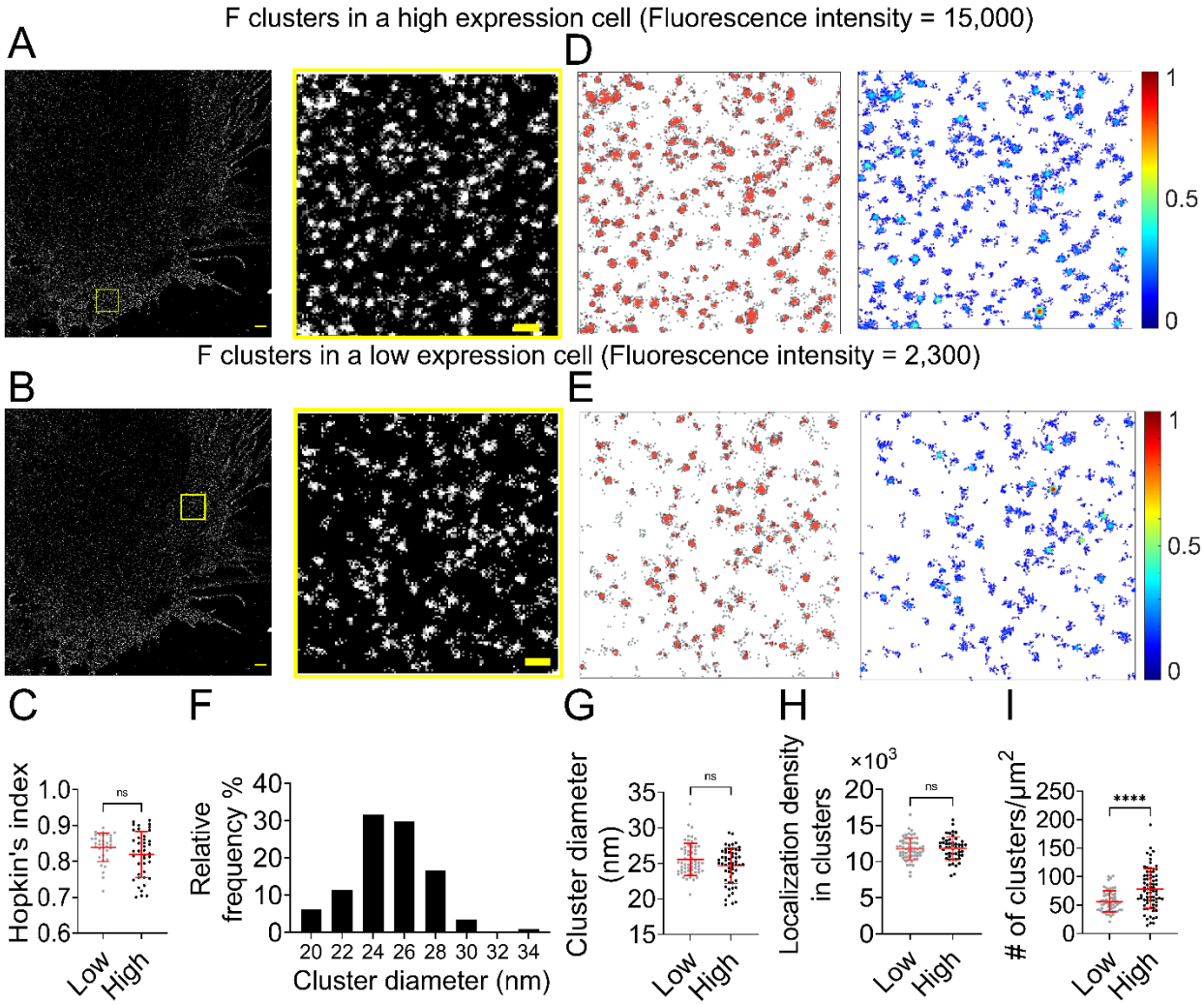

Fig. 1. NiV-F forms regular-sized clusters that are not affected by the surface expression level. *(A and B) Cross-section (Δz = 600 nm) of SMLM images of NiV-F in high-expression (A) and low-expression (B) PK13 cells. Scale bar: 1 μm. The yellow boxed region is enlarged to show the detailed distribution pattern. Scale bar: 0.2 μm. (C) Hopkin's index of the F localizations in low- and high-expression cells. n = 35 and 40. (D and E) Cluster maps (left) and localization density maps (right) of the enlarged regions in A and B. Cluster contours are highlighted with gray lines. Normalized relative density is pseudocolored according to the scale on the right. (F) The percentage distribution of the NiV-F cluster diameter from 13 cells. n = 133. (G) The cluster diameters in low- and high-expression cells. n = 58 and 56. (H) The localization density (# of localizations per μm^2) within clusters in low- and high-expression cells. n = 58 and 50. (I) The number of clusters per μm^2 in low- and high-expression cells. n = 59 and 74. The cut-off fluorescence intensity for low- and high-expression cells is 8000 (Arb. Unit). Sample size n is the number of total regions from 6-8 cells. Bars represent mean ± SD. P value was obtained using the Mann-Whitney test. ns: p > 0.05; * p<0.01; ** p<0.001; *** p<0.0001.*

The NiV-F nanoclusters are not affected by NiV-F cleavage.

NiV-F is synthesized in host cells as inactive precursor F_0 and cleaved by cellular proteases cathepsin L and cathepsin B in the endosomes at an acidic pH to generate the fusion-active, disulfide-linked F_1-F_2 construct. The F_1-F_2 is subsequently recycled to the cell surface to induce cell-cell fusion and incorporated into virus particles. We hypothesized that the F_0 precursor and the F_1-F_2 active forms co-existed in the same clusters on the cell surface. To test this hypothesis, we used a pan-cysteine cathepsin inhibitor E64d to inhibit the NiV-F cleavage. E64d inhibited the cell-cell fusion induced by NiV-F and NiV-G in HeLa cells (Fig. S3), agreeing with the previous fusion inhibitory effects in Vero and MDCK cells[5,6]. Our SMLM images show that E64d treatment does not result in any significant change in the clustering of NiV-F in HeLa cells (Fig. 2A). The clustering extent of NiV-F was not altered by the E64d treatment, as shown by comparable Hopkin's indices (Fig. 2B). Additionally, quantitative parameters of the nano-organization such as percentage of localizations in clusters (Fig. 2C), relative density (Fig. 2D), cluster size (Fig. 2E), and the total density of the regions (Fig. 2F). Our data show that clusters formed by non-cleaved NiV-F in cells treated by E64d are similar to those formed by a mixture of cleaved and non-cleaved NiV-F in the control cells, suggesting that F cleavage does not alter F clustering on the cell membrane. These data support our hypothesis that the non-cleaved precursor F_0 and cleaved F_1-F_2 coexist in the same cluster on the cell membrane.

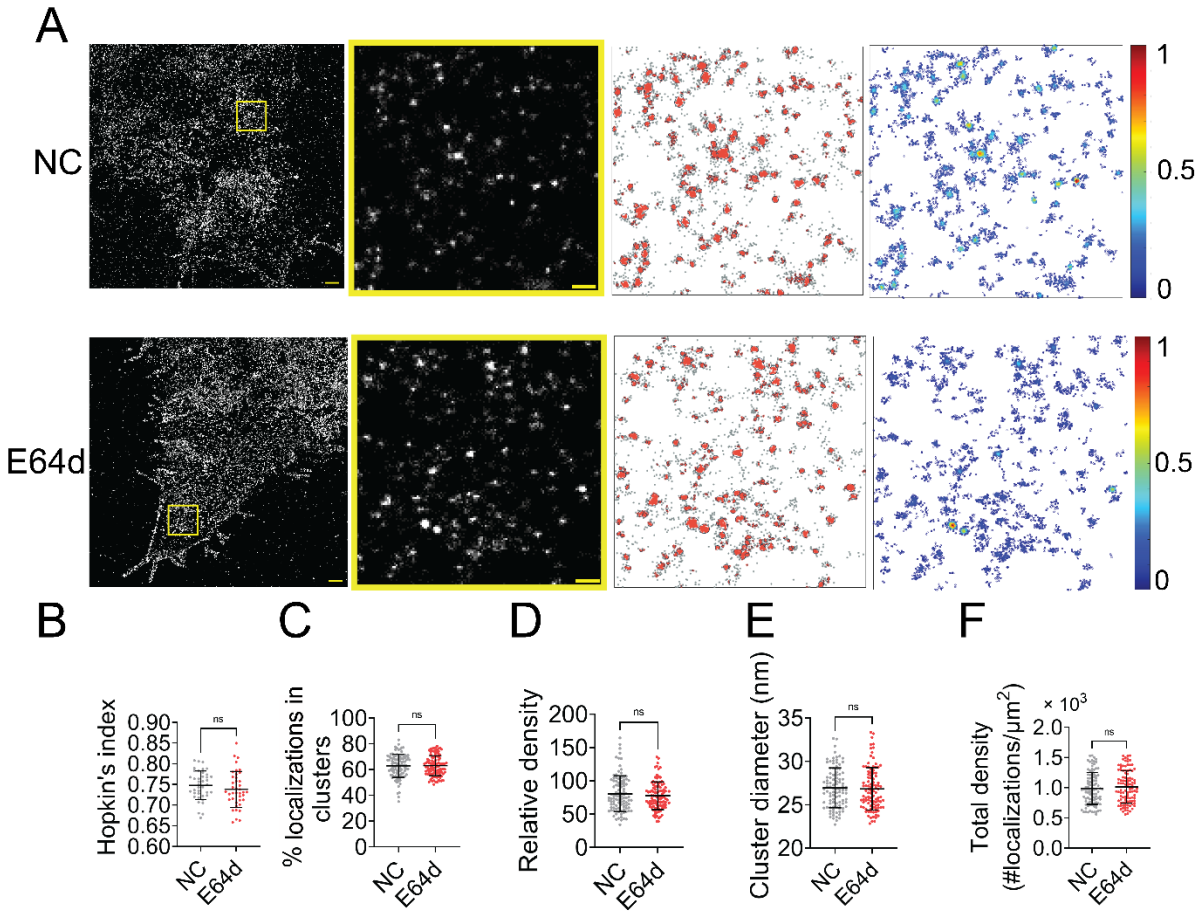

Fig 2. Endosomal cleavage does not affect the nanoscale distribution of NiV-F. *(A) First column: Cross-section (Δz = 600 nm) of SMLM images of NiV-F in HeLa cells untreated (NC)*

*and treated with 20 μM E64d (E64d). HeLa cells were co-transfected by expression plasmids coding for NiV-G and NiV-F. Twenty μM E64d or the same volume of solvent methanol was added to cells at 2 hrs post-transfection. Scale bar: 1 μm. Second column: The yellow boxed region in the first column is enlarged to show individual clusters. Scale bar: 0.2 μm. Third column: Cluster maps from the enlarged regions. Fourth column: Localization density maps show the normalized relative density of the enlarged regions. (B-F) Quantitative analyses of NiV-F clusters formed in HeLa cells without (NC) and with (E64d) the E64d treatment: (B) Hopkin's index, n = 40 and 40; (C) percentage of localizations in clusters, n = 101 and 101; (D) relative density, n = 100 and 103; (E) average cluster diameters, n = 100 and 101; (F) total density of the region, n = 101 and 102. Bars represent mean ± SD. p value was obtained using Mann-Whitney test. ns: p > 0.05; * p<0.01; ** p<0.001; *** p<0.0001. Sample size n is the number of total regions from 4-10 cells.*

Mutations destabilizing the NiV-F hexamer-of-trimer assembly alter its nano-organization on plasma membrane.

We noticed that the uniformity in the NiV-F cluster morphology resembled the hexameric assembly of soluble NiV-F decorated by GCN4[10]. Next, we investigated whether NiV-F clusters were stabilized by the hexameric interface. As reported, L53D and V108D mutants destabilize the hexameric interface and demonstrate decreased membrane fusion ability; Q393L stabilizes the hexameric interface and demonstrates increased fusion ability. We inserted the FLAG tag into the ectodomains of these mutants at the same position as that of the NiV-F. We verified that the relative fusion ability to their F-WT counterpart was comparable between the FLAG-tagged and untagged mutants (Fig. S4A and S4B)[10]. The FLAG-tagged mutants showed similar CSE levels to NiV-F (Fig. S4C). All mutants showed some levels of processing, although the cleavage of L53D was the least efficient comparing to F-WT and other mutants (Fig. S4D).

NiV-F mutants L53D, V108D, and Q393L were expressed on PK13 cells and subjected to SMLM imaging. The images show that clusters formed by L53D and V108D are smaller and more dispersed than those of the F-WT and Q393L (Fig. 3A). The Hopkin's index for Q393L is significantly higher than that of F-WT, while the Hopkin's indices for L53D and V108D are slightly lower than that of F-WT (Fig. 3B). Consistently, a lower percentage of L53D and V108D localizations are segregated into clusters than that of F-WT, while a similar percentage of Q393L and F-WT localizations form clusters (Fig. 3C). Our analysis also shows that L53D and V108D form smaller clusters compared to the F-WT. The Q393L clusters are of a similar size to that of F-WT (Fig. 3D). In addition, clusters of L53D and V108D are less packed than that of F-WT, with 48-, 49-, and 55-fold denser than the total localization density in the region, respectively (Fig. 3E). The clusters of Q393L are not significantly denser than that of F-WT (Fig. 3E). The total density of localizations and the total CSE levels for all constructs are comparable (Fig. 3F and Fig. S4C), suggesting that differences in clustering are not due to variable numbers of localizations or levels of expression. Collectively, these data show that the mutations destabilizing the hexameric interface (L53D and V108D) make NiV-F localizations more dispersed and form smaller and less packed clusters. Q393L that stabilizes the hexameric interface promotes the clustering of NiV-F localizations (Fig. 3B), but does not significantly alter the organization and morphology of individual clusters (Fig. 3C-F). These data suggest that the NiV-F clusters are susceptible to mutations at the hexameric interface. Considering that the uniformed cluster size is similar to the assemblies formed by the soluble GCN4-NiV-F, we propose that NiV-F may organize into hexamer-of-trimer on the plasma membrane.

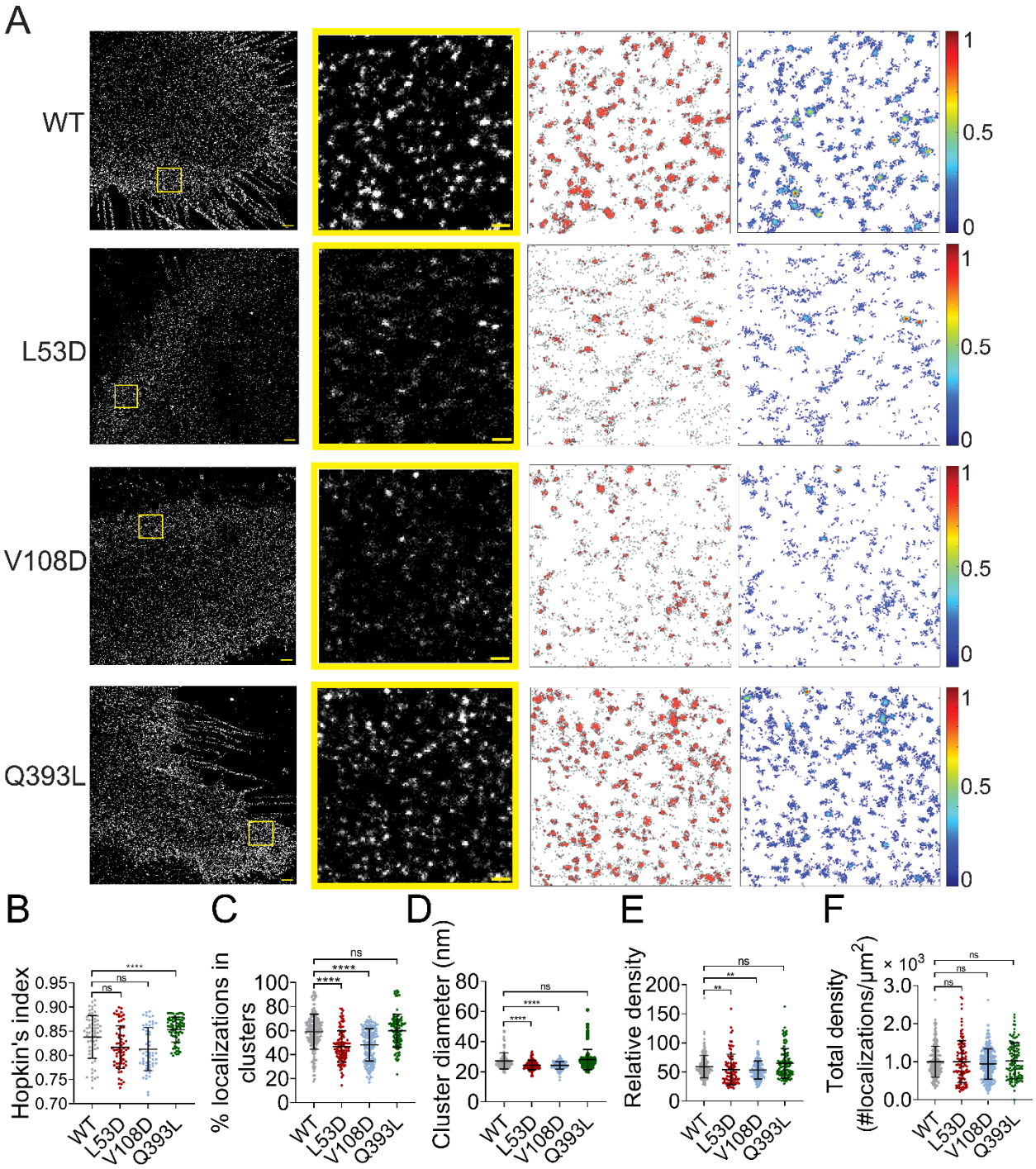

Fig. 3. Mutations at the NiV-F hexameric interface affect its nano-organization. *(A) First column: Cross-section (Δz = 600 nm) of SMLM images of the FLAG-tagged NiV-F-WT (WT), L53D, V108D, and Q393L on PK13 cell membrane. Scale bar: 1 μm. Second column: The yellow boxed regions in the first column are enlarged to show individual clusters. Scale bar: 0.2 μm. Third row: Cluster maps from enlarged regions. Fourth column: Localization density maps show normalized relative density of the enlarged regions. (B-F) Quantitative analyses of the distribution of the FLAG-tagged NiV-F constructs: (B) Hopkin's index, n = 57-70; (C) Percentage of localizations in clusters, n = 106-198; (D) Average cluster diameters, n = 106-196; (E)*

*Relative density, n = 90-187; (F) total density of the region (a ratio of total localizations in a region to the size of the region), n = 105-242. Bars represent mean ± SD. Sample size n is the number of total regions from 11-20 cells. p value was obtained using Mann-Whitney test. ns: p > 0.05; * p<0.01; ** p<0.001; *** p<0.0001.*

Mutations at the NiV-F hexameric interface affect its distribution on the VLP membrane. To further investigate the organization of F mutants in viral membranes, we imaged the FLAG-tagged NiV-F constructs on VLPs produced by 293T cells expressing NiV-M-GFP, NiV-G, and NiV-F-WT, L53D, V108D, or Q393L mutants. The western blot analysis of NiV-F constructs on the VLPs (Fig. 4A). The L53D and V108D on VLPs are less cleaved compared to that of the F-WT and Q393L, as suggested by the weaker NiV-F_2 bands (Fig. 4A). The incorporation of NiV-F is comparable among the NiV-F constructs (Fig. 4A). Notably, the incorporation of NiV-G is largely abrogated in the VLPs that expressing L53D (Fig. 4A).

To probe the organization of NiV-F constructs on VLPs, the F-constructs on VLP membranes were stained using Alexa Fluor 647 and subjected to SMLM imaging. The GFP fluorescence on NiV-M was used to locate the VLPs. Fig. 4B shows that F-WT and F-Q393L form distinctive clusters, while localizations of L53D and V108D are more dispersed on a z = 100 nm projection. This agrees with their distributions on the plasma membrane (Fig. 3A). To gain a quantitative insight into the distribution of the F constructs on the three-dimensional (3D) VLPs, we used an algorithm named OPTICS (Ordering Points To Identify Clustering Structure)[16]. To identify clusters, the OPTICS algorithm sorts out the localizations by calculating the reachability distance between two adjacent localizations in a propagative manner and generates a sequence of the ordered localizations[16]. In the plot of reachability distance vs. the sequence of ordered localizations, a sudden increase in the reachability distance marks the cutoff of a cluster (Fig. S5A). The shade between neighboring peaks represents localizations that are classified in one cluster (Fig. S5A). OPTICS can identify sub-clusters on a 3D VLP that may not be recognized by DBSCAN that uses one fixed parameter for the entire dataset. Fig. S5B shows the OPTICS plots of the localizations of F-WT and mutants on representative VLPs (Fig. 4B). The noticeable kinks suggest that F-WT and Q393L form distinctive clusters on VLPs, while the irregular, small kinks indicate that L53D and V108D are more dispersed and form smaller clusters on VLPs (Fig. 4B and Fig. S5B). To gain a population insight on the nano-organization of the F constructs on VLPs, we developed a one-dimensional convolutional neural network (1D CNN) to classify the ordered sequence of reachability distances of the NiV-F localizations obtained by the OPTICS algorithm[17]. The distribution patterns of the localizations of the F-WT and Q393L partition into one category, and L53D and V108D in another (Fig. 4C). These results indicate that L53D and V108D form smaller and more dispersed clusters than F-WT and Q393L on the VLP membranes, agreeing with that of the plasma membrane (Fig. 3). Our results indicate that the trimer-trimer interaction at the hexameric interface is key in stabilizing the nano-organization of NiV-F on both cell and viral membranes, and NiV-F do not seem to rearrange during the incorporation into VLPs. Nonetheless, our data do not rule out the possibility that the association of nucleocapsids with the plasma membrane during assembly may reorganize NiV-F on the authentic virus membranes.

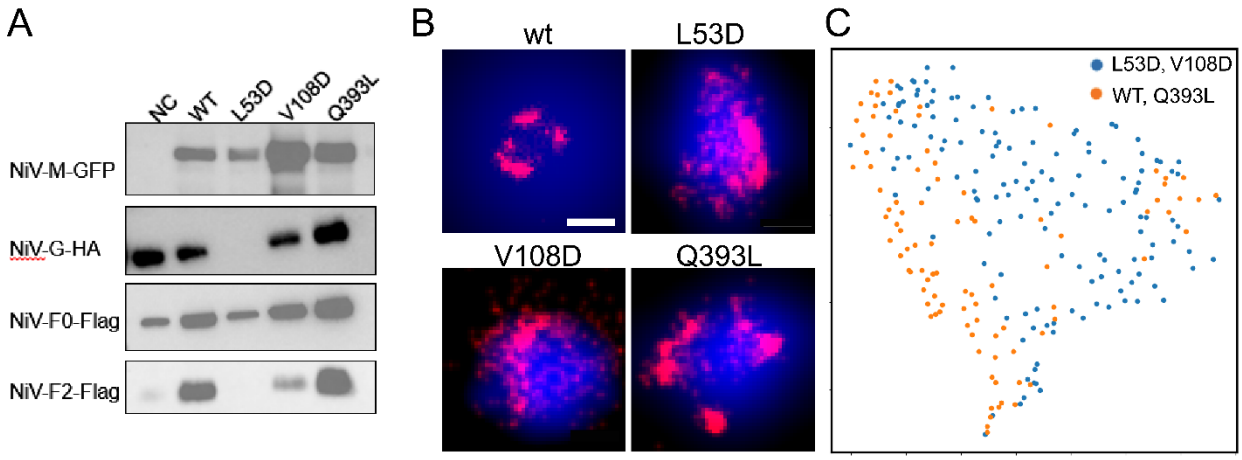

Fig. 4. The distribution and organization of NiV-F constructs in VLPs. *(A). The incorporation of F-WT and mutants in VLPs. NiV-M-GFP, G-HA, and FLAG-tagged F-WT or mutants were transfected to 293T cells. The supernatants were collected at 48 hrs post-transfection and analyzed on SDS-PAGE followed by western blotting. NiV-M was probed by polyclonal goat anti-GFP, NiV-G polyclonal rabbit anti-HA, F_0 and F_2 M2 monoclonal mouse anti-FLAG antibody. (B) Cross-section (Δz = 100 nm) of SMLM images of the FLAG-tagged NiV-F-WT (WT), L53D, V108D, and Q393L on individual VLPs. Scale bar: 0.2 μm.* (C) The classification of the ordered sequence of reachability distances of the NiV-F constructs localizations. Orange: F-WT and Q393L; Blue: L53D and V108D.

The NiV-F clusters are dispersed upon the disruption of the interactions between transmembrane domains (TMD). Evidence shows that TMD of class I fusion protein can self-associate in the absence of the rest of the protein and is important for membrane fusion[18]. Previous studies show that mutations in the Leucine-Isoleucine Zipper (LI zipper) motif lead to the dissociation of an HeV-F TMD-derived peptide, decreased stability, and the fusion ability of the whole HeV-F protein[19]. As the TMD domains of the NiV- and HeV-F demonstrate a 94% similarity, we mutated leucine (488 and 509) and isoleucine (495 and 502) residues of the LI zipper in NiV-F TMD to alanine (LI4A) (Fig. S6A). Similar to their counterparts of HeV-F, the NiV-F-LI4A showed a decreased F processing (Fig. S6B), cell-cell fusion activity (Fig. S6C and S6D), and CSE levels (Fig. S6E)[19]. Visual inspection of the images suggests that LI4A forms bigger clusters than F-WT (Fig. 5A). However, the LI4A seems less likely to cluster than F-WT, indicated by a lower Hopkin's index (Fig. 5B). Similarly, the portion of LI4A localizations partitioned into clusters is slightly lower than that of WT (Fig. 5C). Interestingly, we noticed that clusters formed by LI4A are significantly bigger (Fig. 5D) than that of F-WT and with a similar localization density within the clusters (Fig. 5E). The data suggest that interactions between TMDs of NiV-F monomers play a role in stabilizing its nano-organization. Dissociation of TMDs by mutations may result in increased space between F monomers and thus leads to bigger clusters on the cell membrane.

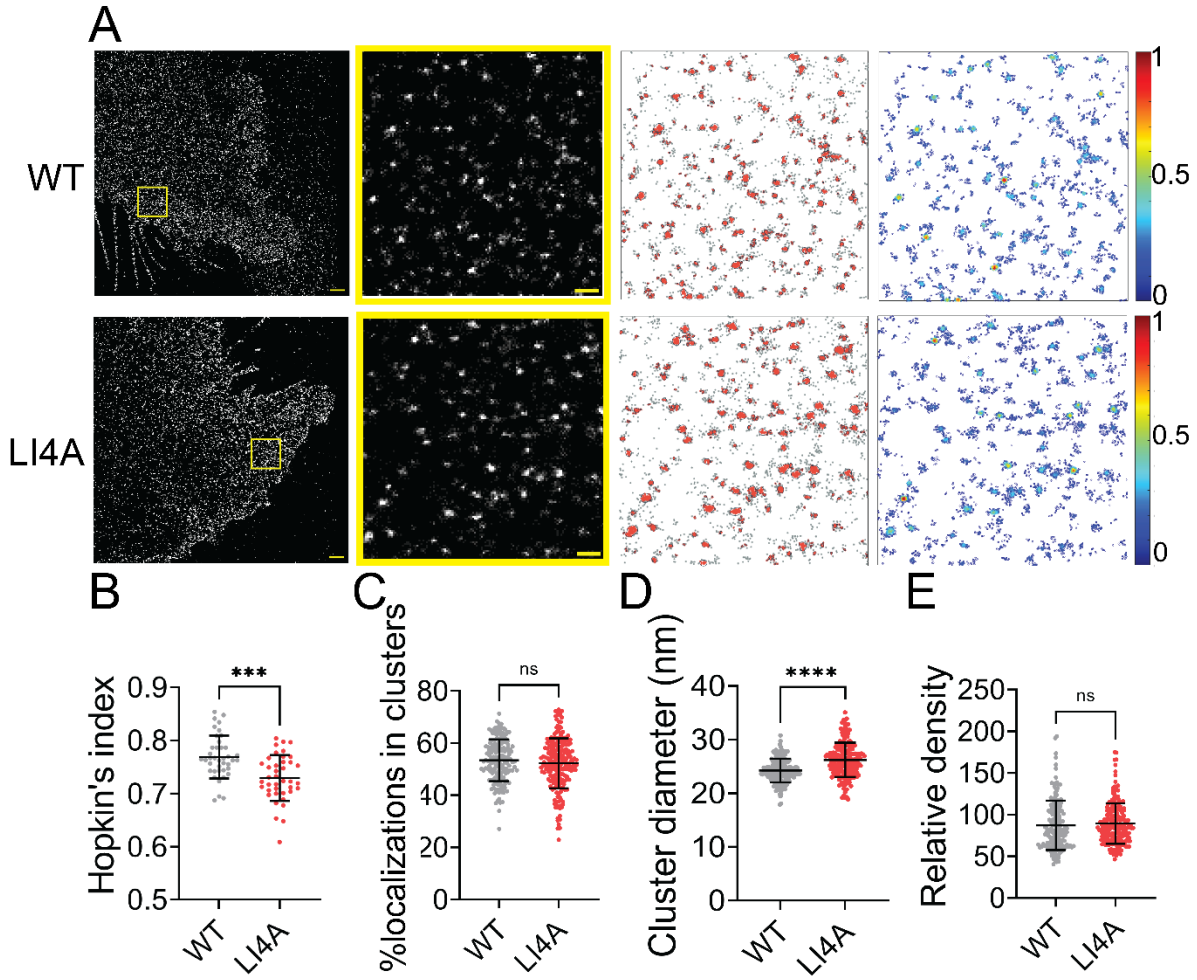

Fig. 5. Mutations in the LI zipper of the NiV-F transmembrane domain disturbs the NiV-F distribution. *A) First column: Cross-section (Δz = 600 nm) of SMLM images of the FLAG-tagged NiV-F-WT (WT) and NiV-F-LI4A (LI4A) mutant on PK13 cell membrane. Scale bar: 1 μm. Second column: The yellow boxed region in the first column is enlarged to show individual clusters. Scale bar: 0.2 μm. Third column: Cluster maps from enlarged regions. Fourth column: Localization density maps show normalized relative density of the enlarged regions in the second row. (B-F) Quantitative analyses of the WT and LI4A clusters: (B) Hopkin's index, n=40 and 40 (C) Percentage of localizations in clusters, n = 171 and 211; (D) Average cluster diameters, n = 171 and 211; (E) Relative density, n = 166 and 211. Bars represent mean ± SD. p value was obtained using Mann-Whitney test. ns: p > 0.05; * p<0.01; ** p<0.001; *** p<0.0001. Sample size n is the number of total regions from 13-16 cells.*

The NiV-F nanoclusters are stabilized by endocytosis components.

NiV-F can be endocytosed for endosomal cleavage. Next, we investigated whether NiV-F clusters are stabilized during endocytosis. NiV-F contains an endocytosis sorting signal YSRL and an additional YY motif at its cytoplasmic tail (Fig. S7A). Mutation of these tyrosine residues to alanine almost diminished NiV-F cleavage (Diederich et al., 2005). A FLAG-tagged NiV-F-YA construct containing the aforementioned mutations resulted in significantly less F_2 band than F-WT (Fig. S7B) and completely abrogated cell-cell fusion in 293T cells (Fig. S7C and S7D),

309 although the CSE levels were comparable to that of F-WT (Fig. S7E). By visually inspecting the
310 SMLM images, we noticed that F-YA was less clustered than that of F-WT (Fig. 6A). Indeed, the
311 Hopkin's analysis suggests that F-YA is less clustered than F-WT (Fig. 6B). The DBSCAN
312 analysis shows that a lower percentage of F-YA localizations segregate into clusters (Fig. 6C)
313 than that of the F-WT, and clusters formed by F-YA are smaller (Fig. 6D) and less dense (Fig.
314 6E) than that of the F-WT. Notably, there is no significant difference in the total density for F-YA
315 and F-WT SMLM images (Fig. 6F), indicating that the differences in cluster organizations do not
316 result from overall protein expression or the stochastic blinking properties of the fluorophore.
317 These results suggest that the endocytosis sorting signal of NiV-F may facilitate the enrichment
318 of NiV-F into clusters on the cell surface, preparing them for endosomal cleavage and/or
319 incorporation into viruses.

320 It is established that the YxxΦ sorting signal on the endocytosis cargo is bound and enriched by
321 the heterotetrameric adaptor protein (AP) complexes, which further recruit the assembly of the
322 clathrin coat[20,21]. We hypothesize that the clustering of NiV-F is promoted by the assembly of the
323 clathrin coat via the NiV-F-AP-2 interactions. As suggested by a yeast two-hybrid analysis, NiV-
324 F interacts with μ1, μ2, μ3 and μ4 subunits of the AP complexes AP-1, AP-2, AP-3, and AP-4,
325 and mutations of Y525, Y542, and Y543 almost completely abolished the interaction between
326 AP-2 and NiV-F[22]. Indeed, the co-immunoprecipitation assay shows that less AP2μ2 is pulled
327 down by F-YA than that of F-WT, suggesting that F-YA has a reduced interaction with AP-2 (Fig.
328 S7F). Next, we examined the NiV-F clusters in HeLa cells treated by the endocytosis inhibitor
329 pitstop2. Pitstop2 blocks clathrin-mediated endocytosis by obstructing the binding of the
330 accessory protein (*e.g.* AP-2) and the clathrin terminal domain, and potentially preventing the
331 assembly of the clathrin coat[23]. The SMLM images (Fig. 6G) show that the NiV-F localizations
332 are more dispersed upon pitstop2 treatment, agreeing with the lower Hopkin's index (Fig. 6H)
333 and a smaller percentage of localizations in clusters (Fig. 6I) in pitstop2 treated group compared
334 to that of the control group. Interestingly, we noticed that the NiV-F clusters in pitstop2 treated
335 cells were larger than the control cells (Fig. 6K), although with similar densities (Fig. 6J). The
336 total density is consistent between the pitstop2 treated and control groups (Fig. 6L). The overall
337 dispersed NiV-F distribution upon pitstop2 treamtnet may potentially be caused by the disrupted
338 assembly of clathrin coat. In combination, these results suggest that the enrichment of NiV-F by
339 AP-2 and the subsequent assembly of the clathrin-coated endosomes are important in
340 stabilizing the F clusters on cell membranes. We envision that the endocytosis components may
341 also facilitate the NiV-F clustering in virus particles as previous proteomic studies show the
342 presence of endocytosis related proteins, such as clathrin, AP-2, and dynamin in NiV VLPs[24–26].

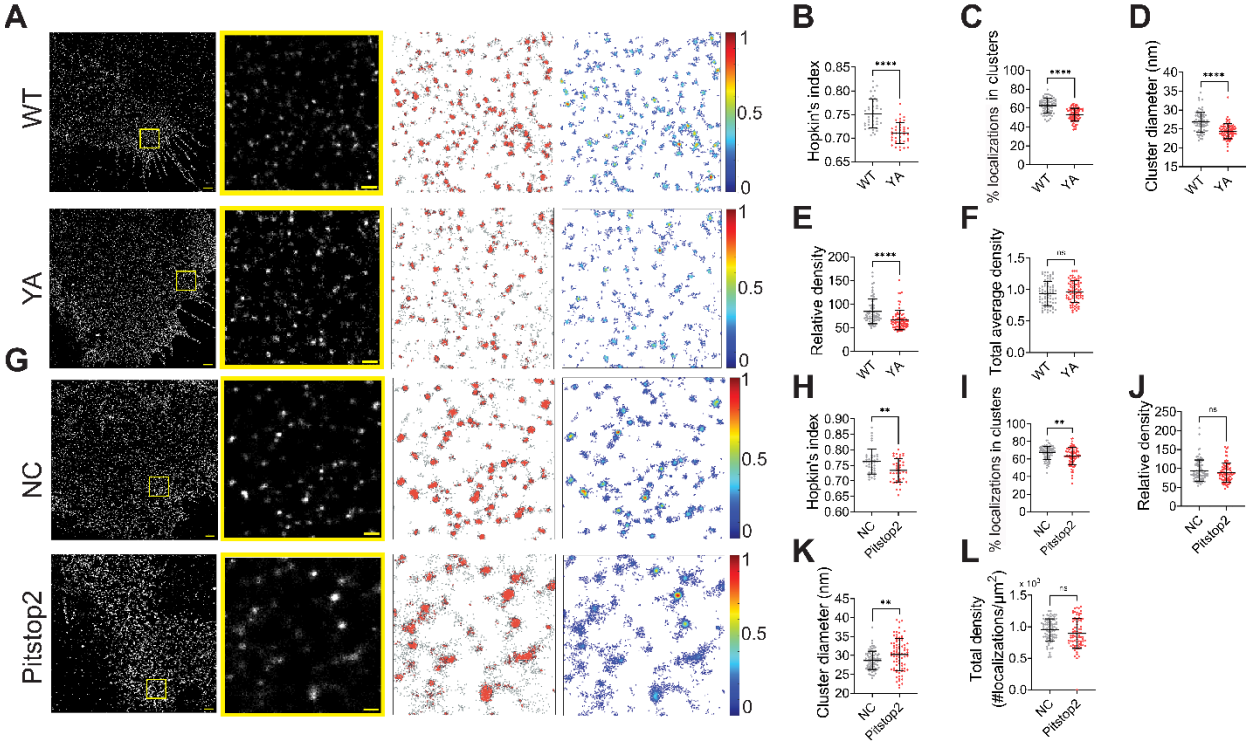

Fig. 6. The NiV-F nanoclusters are stabilized by endocytosis components. *(A) First column: Cross-section (Δz = 600 nm) of SMLM images of the FLAG-tagged NiV-F-WT (WT) and NiV-F-YA (YA) mutant on PK13 cell membrane. Scale bar: 1 μm. Second column: The yellow boxed region in the first column is enlarged to show individual clusters. Scale bar: 0.2 μm. Third column: Cluster maps from enlarged regions. Fourth column: Localization density maps show normalized relative density of the enlarged regions in the second row. (B-F) Quantitative analyses of the WT and YA clusters: (B) Hopkins index of WT and YA, n = 40 and n = 40; (C) Percentage of localizations in clusters, n = 72 and 77; (D) Average cluster diameters, n = 72 and 77; (E) Relative density, n = 71 and 76; (F) total density of the region, n = 72 and 77. (G) First column: Cross-section (Δz = 600 nm) of SMLM images of the FLAG-tagged NiV-F-WT treated without (NC) and with pitstop2 (pitstop2) on HeLa cell membrane. Scale bar: 1 μm. Second column: The yellow boxed region in the first column is enlarged to show individual clusters. Scale bar: 0.2 μm. Third column: Cluster maps from enlarged regions. Fourth column: Localization density maps show normalized relative density of the enlarged regions in the second row. (H-L) Quantitative analyses of NiV-F without (NC) and with pitstop2 (pitstop2): (H) Hopkins index, n = 40 and n = 40; (I) Percentage of localizations in clusters, n = 82 and 85; (J) Relative density, n = 82 and 81; (K) Average cluster diameters, n = 82 and 81; (L) total density of the region, n = 82 and 81. Bars represent mean ± SD. p value was obtained using Mann-Whitney test. ns: p > 0.05; * p<0.01; ** p<0.001; *** p<0.0001. Sample size n is the number of total regions from 4-9 cells.*

Discussion.

Here we used SMLM to resolve the arrangement and organization of NiV-F on the biological membranes at a resolution of 10 nm. Our data supports the following conclusions: 1) NiV-F is organized into nanoclusters on the biological membranes and this organization is independent of the protein expression level or endosomal cleavage; 2) the NiV-F nano-organization is

susceptible to mutations at the trimer interface on the NiV-F ectodomain and the putative oligomerization motif on the transmembrane domain; 3) NiV-F sequestered in nanocluaters favors membrane fusion activation; 4) the interactions among NiV-F, the AP-2 complex, and the clathrin coat assembly stabilize the NiV-F clusters. We propose that the NiV-F nanoclusters are the fundamental unit of the NiV fusion machinery, and this organization facilitates membrane fusion triggering by a mixed population of NiV-F molecules with varied degrees of cleavage and opportunities of interacting with NiV-G/receptor complex.

The nano-organization of NiV-F informs the coordinated membrane fusion triggering by a mixed population of NiV-F. This notion is supported by the following observations from this and previous studies: 1) NiV-F molecules form distinctive, regular-sized nanoclusters on the cell and virus membranes (Fig. 1A-E); 2) the cleaved, active F co-exist with the noncleaved, inactive F in a nanocluster, as suggested by that the NiV-F nanoclusters are resistant to the cathepsin inhibitor, E64d (Fig. 2); 3) the NiV-F and G are segregated into different clusters [11]; and 4) the full-length NiV-F and -G proteins do not show stable interactions either before or after ephrinB2 activation [12]. These observations indicate that the NiV-F triggering may be a result of transient interactions between the F molecules at the edge of the clusters with the adjacent ephrinB2/G complex. Moreover, we observed that the NiV-F sequestering into clusters is favorable for membrane fusion activation (Fig. 3 and 5), highlighting the importance of the spatial arrangement of NiV-F in its fusion activity. Therefore, it is likely that the triggered, fusion-active NiV-F at the cluster peripheral can facilitate other F molecules in the same cluster to fulfill the conformational changes, and thus maximize the energy to merge the opposing membranes.

The nano-organization of NiV-F reveals the fundamental unit of NiV fusion machinery. Previous study revealed a hexamer-of-trimer assembly of soluble, GCN4-decorated, prefusion NiV-F. Using SMLM, we estimated that the NiV-F clusters had a diameter between 24-26 nm (Fig. 1F). This estimation agrees with the size of the hexameric soluble NiV-F-GCN4 assemblies[10]. Notably, the density of clusters (Fig. 1I), but not the size and localization density of individual clusters (Fig. 1G and H), is affected by the surface expression levels of NiV-F, implying that the NiV-F clusters are highly regulated and a fundamental functional unit. Nonetheless, a collaborative effort of multiple copies of viral envelope proteins is favorable for overcoming the energy barrier required for membrane fusion. Nanoclusters formed by viral glycoproteins have been observed for HIV-1[27,28], Herpes virus[29], and Influenza virus[30]. The viral restriction factor, serine incorporator protein 5 (SERINC5), inhibits HIV-1 fusion by disrupting the HIV env nanoclusters, highlighting the importance of the nanoclusters in the function of the viral glycoproteins[31]. More interestingly, the NiV-F distribution becomes more dispersed, characterized by smaller and less dense clusters, upon the mutation of two key residues, L53 and V108, at the hexameric interface, suggesting that the NiV-F clusters are likely to be the hexamer-of-trimer assemblies on the cell and viral membranes (Fig. 3 and 4).

We also identified that the endosomal components as key host factors in maintaining the NiV-F nano-organization on the cell membrane. Our data suggest that both the disruption of the F/AP-2 interaction and the inhibition of clathrin assembly by pitstop2 result in dispersed NiV-F distribution. AP-2 is the key adaptor of clathrin-mediated endocytosis. It binds cargo and PtdIns(4,5)P_2 -containing membrane via multiple interface, and undergoes conformational changes to append to the clathrin lattice[23,32]. Our data indicate that AP-2-NiV-F interaction can enrich and strengthen the F nanoclusters (Fig. 6A-F and Fig. S7F), and potentially facilitate the uptake of NiV-F by endocytosis. It is reported that the clustering of CD44, modulated by *N*-

414 glycosylations, facilitates the uptake of CD44 by endocytosis. Furthermore, the assembly of the
415 clathrin coat at the plasma membrane may also strengthen the F clusters, because pitstop2 that
416 inhibits the clathrin-coat assembly by blocking the clathrin terminal domain[23] prevents the
417 cluster formation of NiV-F. It is plausible that both clathrin and AP-2 facilitate NiV-F clustering on
418 cell and virus membranes because of the similar organization of F on virus and cell membranes
419 and the presence of clathrin and AP-2 in VLPs[24,26].

420 In conclusion, our observations provide direct evidence on the nano-organization and
421 distribution of NiV-F on the cell and viral membranes and shed lights to the fusion activation
422 mechanisms. It would be interesting to analyze the reorganization of the NiV-F clusters upon
423 triggering by the NiV-G/receptor complex on live cell membranes by combining single-molecule
424 imaging and the supported lipid bilayer technologies[12]. Due to technical challenges, we cannot
425 obtain an exact number of NiV-F molecules in NiV-F clusters. It would be interesting to pinpoint
426 the numbers of NiV-F required for membrane fusion activation on cell and virus surface, and this
427 could potentially facilitate the vaccine design. Additionally, elucidating host factors that maintain
428 NiV-F clusters and the interacting motif in NiV-F may represent a new therapeutic strategy for
429 NiV infections.

430 **Materials and Methods.**

Reagent type	Designation	Source or reference	Identifiers	Additional information
Cell line	HEK293T	ATCC	CRL-3216	
Cell line	PK13	ATCC	CRL-6489	
Cell line	HeLa cells	ATCC	CCL-2	
DNA plasmid	NiV-F-FLAG and mutants	This paper		The FLAG tag was inserted after residue 104 of the codon-optimized NiV-F (genebank accession no. AY816748.1). The hexameric interface mutants (Fig. 3)[10], and LI4A mutant (Fig. 5)[19], and YA mutant (Fig. 6)[6], were constructed as previously published.
DNA plasmid	NiV-F-HA	This paper		The HA tag was inserted after residue 104 of the codon-optimized NiV-F (genebank accession no. AY816748.1).
DNA plasmid	NiV-G-HA	Liu et al. 2018[11]		

DNA plasmid	NiV-M-GFP	Liu et al. 2018, Wang et al. 2010 [11,33]		
DNA plasmid	AP2μ2-mCherry	Christien Merrifield	Addgene 27672	
Chemical compounds, drug	E64d	Sigma-Aldrich	E8640-250UG	20uM
Chemical compounds, drug	Pitstop2	Sigma-Aldrich	SML1169-5MG	30uM
Antibody	Anti-FLAG mouse monoclonal	Sigma-Aldrich	F1804	IF, SMLM: 1:100, Flow: 1:200; WB: 1:500-1:5,000
Antibody	Anti-HA rabbit polyclonal antibody	Biolegend	902301	IF: 1:900 WB: 1:2,000
Antibody	Anti-GFP goat polyclonal antibody	Abcam	Ab5450	WB: 1:1000
Antibody	Anti-mCherry rabbit polyclonal antibody	Abcam	Ab167453	WB: 1:2000
Antibody	Anti-mouse donkey polyclonal antibody, Alexa Fluor® 647 conjugated	Invitrogen	A31571	IF and SMLM: 1:400
Antibody	Anti-rabbit donkey polyclonal antibody, Alexa Fluor® 488 conjugated	Invitrogen	A21206	IF: 1:400
Antibody	Anti-mouse donkey polyclonal antibody, Alexa Fluor® 488 conjugated	Invitrogen	A21202	Flow: 1:400
Antibody	Anti-goat donkey polyclonal antibody, HRP conjugated	Jackson Immunoresearch	705-035-147	WB: 1:5,000
Antibody	Anti-mouse goat polyclonal antibody, HRP conjugated	Biorad	1705047	WB: 1:5,000

Antibody	Anti-rabbit goat polyclonal antibody, HRP conjugated	Biorad	1706515	WB: 1:5,000
Commercial assays and kits	µMACS anti-DYKDDDDK starting kit	Miltenyi Biotec	130-101-636	
software	SMLM image reconstruction	Liu et al. 2018[11]		MATLAB Codes are available upon request.
software	ClusDoc	Pageon et al. 2015[15]		Codes were modified to process the data generated in the custom-built SMLM microscope.
software	OPTICS [16]	This paper		C++ Codes are available upon request.
software	One-dimensional convolutional neural network (1D CNN)	This paper		PYTHON Codes are available upon request.
software	Prism Graphpad	Dotmatics		
software	Flowjo	BD		

Cell lines and plasmids.

PK13, HeLa, and HEK293T cells were cultured at 37°C and 5% CO_2 in DMEM (Sigma-Aldrich, D6429) complemented with 10% fetal bovine serum (Invitrogen, 12483-020). Cells were passaged using phosphate-buffered saline (PBS, Invitrogen, 10010-049) and 0.25% Trypsin-EDTA solution (Invitrogen, 25002-072). Cells were monitored routinely for mycoplasma contamination using a mycoplasma detection PCR kit (ABM, G238). A FLAG (NiV-F-FLAG) or HA (NiV-F-HA) tag was inserted after residue 104 of codon-optimized NiV-F in pcDNA3.1 vector. NiV-F-YA, L53D, V108D, Q393L, and LI4A were produced by site-directed mutagenesis using the NiV-F-FLAG in pcDNA3.1 vector as a template[6,10,19]. AP2µ2-mcherry plasmid is a gift from Christien Merrifield (Addgene # 27672). The HA-tagged NiV-G and GFP-tagged NiV-M were constructed previously.

Immunofluorescence (IF) for SMLM.

For SMLM imaging on cells, 1×10^5 PK13 or HeLa cells were seeded on coverslips (Marienfeld #1.5H, 18 mm) coated with 2.5 µg fibronectin (Sigma-Aldrich, F4759-2 mg) in a 12-well plate, and transfected with 1 µg NiV-F variants using lipofectamine 3000 (Invitrogen, L3000015) on the following day. E64d was dissolved in methanol and pitstop2 in DMSO as recommended by the manufacturer. E64d was added to cells at 3 hrs post-transfection for a total treatment time of 15 hrs. Pitstop2 was added to cells at 10 hrs post-transfection for a total treatment time of 8 hrs. At 18 hrs posttransfection, cells were fixed with PBS containing 4% paraformaldehyde (PFA; Electron Microscopy Sciences; 50980487) and 0.2% glutaraldehyde (Sigma-Aldrich, G5882-50

452 ml) for 90 min at room temperature. Cells were treated with signal enhancer image-IT-Fx (Life
453 Technologies, I36933) for 30 min at room temperature, and then blocked using BlockAid (Life
454 Technologies, B10710) for 1 hr at room temperature. The FLAG-tagged NiV-F and mutants were
455 detected by the anti-FLAG mouse monoclonal antibody (Sigma-Aldrich, F1804) and an Alexa
456 Fluor® 647 conjugated donkey anti-mouse secondary antibody (Invitrogen, A31571). Cells were
457 incubated with primary antibody overnight at 4°C, and then with the secondary antibody for 1 hr
458 at room temperature. Each antibody incubation is followed by five PBS washes, 5 min each
459 time. Cells were then fixed in PBS containing 4% PFA for 10 min at room temperature.

460 SMLM setup, imaging, and data analysis.

461 Imaging was performed on a custom-built SMLM. Briefly, the microscope was built upon an
462 apochromatic TIRF oil-immersion objective lens (Nikon, 60x; numerical aperture 1.49). Four
463 lasers were used for excitation: a 639 nm laser (MRL-FN-639, 500 mW) for exciting Alexa Fluor®
464 647, a 532 nm laser (MGL-III-532-300 mW) for exciting cy3B, a 488 nm laser (MBL-F-473-300
465 mW) for exciting GFP, and a 405 nm laser (MDL-III-405-100 mW) for reactivating Alexa Fluor
466 647 and cy3B. The emission fluorescence was separated using appropriate dichroic mirrors and
467 filters (Semrock) and detected by electron multiplying charge-coupled devices (EMCCD; Ixon,
468 Andor). A feedback loop was employed to control the sample drift to <1 nm laterally and 2.5 nm
469 axially.

470 Fluorescence beads (Life technologies, F8799) were added to samples as fiducial markers for
471 drift control. Samples were immersed in oxygen-scavenging buffer supplemented with 50 mM
472 mercaptoethylamine (Sigma Aldrich, 30070-10G). The expression level of the protein of interest
473 in individual cells was determined by measuring the average emission fluorescence intensity of
474 an area of 27×27 μm^2. For SMLM imaging, samples were exposed to a laser power density of 1
475 kW/cm^2 for the 639 nm lasers to activate Alexa Fluor® 647. A total of 40,000 images were
476 acquired at 50 Hz for the reconstruction of one SMLM image. Custom-written software in
477 MATLAB (Mathworks) was used to reconstruct SMLM images. Clusters of NiV-F localizations on
478 cell surface resolved by SMLM were identified and characterized using ClusDoC. The min
479 points and ε were set at 4 and 20, respectively.

480 VLP production and immunofluorescence.

481 To produce NiV VLPs, HEK293T cells were transfected by NiV-F-FLAG or mutants, NiV-G-HA,
482 and NiV-M-GFP at a 9:1:5 ratio by using polyethylenimine (PEI) at 1 mg/ml (Polysciences,
483 23966-100). At 48hrs posttransfection, the supernatant of the cell culture was collected and
484 subjected to ultracentrifugation on a 20% sucrose cushion at 125, 392 rcf for 90 min. The VLP-
485 containing pellets were resuspended in 5% sucrose-NTE buffer. VLPs were bound to 2.5 µg
486 fibronectin-coated 18 mm coverslips at 37°C for 4 hrs, followed by fixation using PBS containing
487 4% PFA and 0.2% glutaraldehyde. The immunofluorescence, SMLM setup, and SMLM imaging
488 for cells were followed to stain and image NiV-F-FLAG and mutants on VLPs using SMLM. A
489 widefield image of GFP was acquired and superimposed on the SMLM image of NiV-F. VLPs
490 were identified as GFP-positive particles. The distribution of NiV-F localizations on VLPs was
491 analyzed by using custom-written OPTICS algorithm based on C++ and Point Cloud Library.
492 The classification of the ordered sequence of reachability distances was performed by using
493 custom written one-dimensional convolutional neural network (1D CNN) based on Python and
494 Tensorflow.

495 SDS-PAGE, and western blot analysis and co-immunoprecipitation.

496 For western blot analysis to confirm the expression of NiV-F-FLAG and mutants, HEK293T cells
497 were seeded in 6-well plate and transfected with 2.5 µg pcDNA3.1 empty vector, NiV-F-FLAG,
498 or mutants. At 28 or 48 hrs posttransfection, cells were lysed in RIPA buffer (Millipore-Sigma,
499 20-188) supplemented with protease inhibitor (Sigma-Aldrich, 11836170001) on ice for 30min.
500 The cell lysates were collected after centrifuge at 16,000 ×g for 20 min at 4°C. The cell lysates
501 were supplemented with 1x SDS loading dye [60 mM Tris-HCl (pH=6.8); 2% SDS; 10% glycerol,
502 0.025% Brophenol blue] and 15 mM DTT (Thermo Scientific, R0861), and heated at 95°C for
503 denature. The denatured cell lysates were loaded into 10% polyacrylamide gels for SDS-PAGE.
504 Proteins were transferred to PVDF membrane, pore size 0.45 µm (Cytiva, GE10600021).
505 Membrane was blocked with 1% Bovine serum albumin (Sigma-Aldrich, A9647-50G) in PBS
506 and incubated with anti-FLAG mouse monoclonal antibody (Sigma-Aldrich, F1804). An HRP-
507 conjugated goat anti-mouse secondary antibody and the clarity Western ECL substrate (Biorad,
508 1705060) were used for protein detection. Images were acquired using Chemic Doc MP
509 Imaging System (BioRad).

510 For co-immunoprecipitation experiments, HEK293T cells were transfected with the following
511 combinations 1) 2.3 µg empty pcDNA 3.1 vector and 0.2 µg AP2µ2-mcherry, 2) 0.2 µg AP2µ2-
512 mcherry and 2.3 µg NiV-F-FLAG, and 3) 0.2 µg AP2µ2-mcherry and 2.3 µg NiV-F-YA. At 48 hrs
513 post-transfection, cells from 1 well of a 6-well plate were washed with PBS and lysed in 200 µl
514 lysis buffer provided with the µMACS DYKDDDDK isolation kit, and supplemented with protease
515 inhibitors. Cells were isolated on ice for 30 min. Cell debris was removed by centrifuge at
516 16,000 x g for 20 min at 4°C. 60 µl of cell lysate was set aside for immunoblot analysis, and the
517 rest was used for immunoprecipitation, as recommended by the manufacturer. 6 µl anti-
518 DYKDDDDK microbeads (Miltenyi Biotec, 130-101-591) were added to 140 µl cell lysates and
519 incubated for 30min on ice. µ columns (Miltenyi Biotec, 130-101-591) were prepared according
520 to the manufacturer's instructions. Lysate was run over the columns, and microbeads were
521 washed according to the manufacturer's instruction. 20 µl preheated elution buffer (95°C) was
522 added to the column before eluting the bound immunoprecipitated protein in 50 µl elution buffer.
523 Elute was separated by 10% SDS-PAGE, and proteins were immunoblotted by mouse anti-
524 FLAG and rabbit anti-mcherry primary antibodies. The HRP-conjugated goat anti-mouse and
525 goat anti-rabbit secondary antibodies were used for protein detection.

526 Flow cytometry.

527 HEK293T cells were seeded in 6-well plate and transfected with 2.5 µg pcDNA3.1 empty vector,
528 NiV-F-FLAG, or mutants. Cells were collected in 1 mL phosphate-buffered saline (PBS)
529 containing 10 mM EDTA after 28hrs post-transfection. The collected cells were incubated on ice
530 for 1 h with primary antibody mouse anti-flag diluted in 1:200. Samples were washed twice in
531 fluorescence-activated cell sorting (FACS) buffer (0.1% FBS with PBS). After washing, samples
532 were incubated with fluorescent anti-mouse Alexa Fluor 647 antibody 1:400 on ice for 45 min.
533 After being washed twice again, samples were read on a flow cytometer (Attune® NxT™
534 Acoustic Focusing Cytometer, Thermo Fisher) The results were analyzed through FlowJo. The
535 mean fluorescent intensities (MFI) were normalized to the MFIs of the wt NiV F.

536 Cell-cell fusion.

537 HEK293T cells were seeded in the 12-well plate and transfected with 1µg total DNA of NiV-G
538 and wt-F or mutant-F with a 3:1 ratio using Lipofectamine 3000. Cells were fixed with 4% PFA
539 after 18 hrs post-transfection. Four or more nuclei within a common cytoplasm were considered

syncytium. Syncytia were quantified by counting the number of nuclei in the syncytium per 10 × filed (5 fields are counted per group) under microscope TE2000U.

Acknowledgements. We thank the multiscale imaging facility for instrument use. We thank Dr. Youssef Chebli at McGill University and Dr. David Scriven at the University of British Columbia for the support on laser scanning confocal microscopy and single-molecule imaging. **Funding.** This work is supported by funding from the Canadian Institutes of Health Research to Q.L. (183861) and the Coronavirus Variants Rapid Response Network to Q.L. (175622). **Author contribution:** Conceptualization: Q.W. and Q.L.; Image acquisition: Q.W.; Data analysis and code writing: Q.W., J.L. and Q.L.; Functional analysis: Q.W., Y.L., V.K., G.L.M., J.W.; Resources: Q.L., Supervision: Q.L.; Funding Acquisition: Q.L.. Writing: original draft: Q.W., J.L., and Q.L.; revision: all authors. Competing Interests: The authors declare that they have no competing interests. Code, reagents, and data availability: Custom-written codes are deposited in GitHub or available upon requests. Reagents can be provided by the corresponding author on a completed material transfer agreement. Requests for the reagents and data should be submitted to qian.liu3@mcgill.ca. **Declare of interests.**The authors declare no competing interests.

1. Navaratnarajah, C.K., Generous, A.R., Yousaf, I., and Cattaneo, R. (2020). Receptor-mediated cell entry of paramyxoviruses: Mechanisms, and consequences for tropism and pathogenesis. Journal of Biological Chemistry *295*, 2771–2786. 10.1074/jbc.REV119.009961.

2. Haas, G.D., and Lee, B. (2023). Paramyxoviruses from bats: changes in receptor specificity and their role in host adaptation. Current Opinion in Virology *58*, 101292. 10.1016/j.coviro.2022.101292.

3. Aditi, and Shariff, M. (2019). Nipah virus infection: A review. Epidemiology & Infection *147*, e95. 10.1017/S0950268819000086.

4. Thibault, P.A., Watkinson, R.E., Moreira-Soto, A., Drexler, J.F., and Lee, B. (2017). Zoonotic potential of emerging paramyxoviruses: knowns and unknowns. Adv Virus Res *98*, 1–55. 10.1016/bs.aivir.2016.12.001.

5. Diederich, S., Sauerhering, L., Weis, M., Altmeppen, H., Schaschke, N., Reinheckel, T., Erbar, S., and Maisner, A. (2012). Activation of the Nipah Virus Fusion Protein in MDCK Cells Is Mediated by Cathepsin B within the Endosome-Recycling Compartment. J Virol *86*, 3736–3745. 10.1128/JVI.06628-11.

6. Diederich, S., Moll, M., Klenk, H.-D., and Maisner, A. (2005). The Nipah Virus Fusion Protein Is Cleaved within the Endosomal Compartment *. Journal of Biological Chemistry *280*, 29899–29903. 10.1074/jbc.M504598200.

7. Negrete, O.A., Levroney, E.L., Aguilar, H.C., Bertolotti-Ciarlet, A., Nazarian, R., Tajyar, S., and Lee, B. (2005). EphrinB2 is the entry receptor for Nipah virus, an emergent deadly paramyxovirus. Nature *436*, 401–405. 10.1038/nature03838.

579 8. Liu, Q., Bradel-Tretheway, B., Monreal, A.I., Saludes, J.P., Lu, X., Nicola, A.V., and Aguilar,
580 H.C. (2014). Nipah Virus Attachment Glycoprotein Stalk C-Terminal Region Links Receptor
581 Binding to Fusion Triggering. J Virol *89*, 1838–1850. 10.1128/JVI.02277-14.

582 9. Liu, Q., Stone, J.A., Bradel-Tretheway, B., Dabundo, J., Montano, J.A.B., Santos-Montanez,
583 J., Biering, S.B., Nicola, A.V., Iorio, R.M., and Lu, X. (2013). Unraveling a three-step
584 spatiotemporal mechanism of triggering of receptor-induced Nipah virus fusion and cell
585 entry. PLoS Pathog *9*, e1003770.

586 10. Xu, K., Chan, Y.-P., Bradel-Tretheway, B., Akyol-Ataman, Z., Zhu, Y., Dutta, S., Yan, L.,
587 Feng, Y., Wang, L.-F., Skiniotis, G., et al. (2015). Crystal Structure of the Pre-fusion Nipah
588 Virus Fusion Glycoprotein Reveals a Novel Hexamer-of-Trimers Assembly. PLoS Pathog *11*,
589 e1005322. 10.1371/journal.ppat.1005322.

590 11. Liu, Q., Chen, L., Aguilar, H.C., and Chou, K.C. (2018). A stochastic assembly model for
591 Nipah virus revealed by super-resolution microscopy. Nature Communications *9*, 3050.
592 10.1038/s41467-018-05480-2.

593 12. Wong, J.J., Chen, Z., Chung, J.K., Groves, J.T., and Jardetzky, T.S. (2021). EphrinB2
594 clustering by Nipah virus G is required to activate and trap F intermediates at supported lipid
595 bilayer–cell interfaces. Sci. Adv. *7*, eabe1235. 10.1126/sciadv.abe1235.

596 13. Coelho, S., Baek, J., Graus, M.S., Halstead, J.M., Nicovich, P.R., Feher, K., Gandhi, H.,
597 Gooding, J.J., and Gaus, K. (2020). Ultraprecise single-molecule localization microscopy
598 enables in situ distance measurements in intact cells. Science Advances *6*, eaay8271.
599 10.1126/sciadv.aay8271.

600 14. Dempsey, G.T., Vaughan, J.C., Chen, K.H., Bates, M., and Zhuang, X. (2011). Evaluation of
601 fluorophores for optimal performance in localization-based super-resolution imaging. Nature
602 Methods *8*, 1027–1036. 10.1038/nmeth.1768.

603 15. Pageon, S.V., Nicovich, P.R., Mollazade, M., Tabarin, T., and Gaus, K. (2016). Clus-DoC: a
604 combined cluster detection and colocalization analysis for single-molecule localization
605 microscopy data. Mol Biol Cell *27*, 3627–3636. 10.1091/mbc.E16-07-0478.

606 16. Ankerst, M., Breunig, M.M., Kriegel, H.-P., and Sander, J. (1999). OPTICS: ordering points
607 to identify the clustering structure. SIGMOD Rec. *28*, 49–60. 10.1145/304181.304187.

608 17. Kiranyaz, S., Avci, O., Abdeljaber, O., Ince, T., Gabbouj, M., and Inman, D.J. (2021). 1D
609 convolutional neural networks and applications: A survey. Mechanical Systems and Signal
610 Processing *151*, 107398. 10.1016/j.ymssp.2020.107398.

611 18. Barrett, C.T., and Dutch, R.E. (2020). Viral Membrane Fusion and the Transmembrane
612 Domain. Viruses *12*, 693. 10.3390/v12070693.

613 19. Webb, S., Nagy, T., Moseley, H., Fried, M., and Dutch, R. (2017). Hendra virus fusion
614 protein transmembrane domain contributes to pre-fusion protein stability. Journal of
615 Biological Chemistry *292*, 5685–5694. 10.1074/jbc.M117.777235.

616 20. Bonifacino, J.S., and Neefjes, J. (2017). Moving and positioning the endolysosomal system.
617 Curr Opin Cell Biol *47*, 1–8. 10.1016/j.ceb.2017.01.008.

618 21. Bonifacino, J.S., and Traub, L.M. (2003). Signals for sorting of transmembrane proteins to
619 endosomes and lysosomes. Annu Rev Biochem *72*, 395–447.
620 10.1146/annurev.biochem.72.121801.161800.

621 22. Mattera, R., Farías, G.G., Mardones, G.A., and Bonifacino, J.S. (2014). Co-assembly of
622 Viral Envelope Glycoproteins Regulates Their Polarized Sorting in Neurons. PLOS
623 Pathogens *10*, e1004107. 10.1371/journal.ppat.1004107.

624 23. von Kleist, L., Stahlschmidt, W., Bulut, H., Gromova, K., Puchkov, D., Robertson, M.J.,
625 MacGregor, K.A., Tomilin, N., Pechstein, A., Chau, N., et al. (2011). Role of the Clathrin
626 Terminal Domain in Regulating Coated Pit Dynamics Revealed by Small Molecule Inhibition.
627 Cell *146*, 471–484. 10.1016/j.cell.2011.06.025.

628 24. Johnston, G.P., Bradel-Tretheway, B., Piehowski, P.D., Brewer, H.M., Lee, B.N.R., Usher,
629 N.T., Zamora, J.L.R., Ortega, V., Contreras, E.M., Teuton, J.R., et al. (2019). Nipah Virus-
630 Like Particle Egress Is Modulated by Cytoskeletal and Vesicular Trafficking Pathways: a
631 Validated Particle Proteomics Analysis. mSystems *4*, 10.1128/msystems.00194-19.
632 10.1128/msystems.00194-19.

633 25. Pentecost, M., Vashisht, A.A., Lester, T., Voros, T., Beaty, S.M., Park, A., Wang, Y.E., Yun,
634 T.E., Freiberg, A.N., Wohlschlegel, J.A., et al. (2015). Evidence for ubiquitin-regulated
635 nuclear and subnuclear trafficking among Paramyxovirinae matrix proteins. PLoS Pathog
636 *11*, e1004739. 10.1371/journal.ppat.1004739.

637 26. Vera-Velasco, N.M., García-Murria, M.J., Sánchez Del Pino, M.M., Mingarro, I., and
638 Martinez-Gil, L. (2018). Proteomic composition of Nipah virus-like particles. J Proteomics
639 *172*, 190–200. 10.1016/j.jprot.2017.10.012.

640 27. Chojnacki, J., and Eggeling, C. (2018). Super-resolution fluorescence microscopy studies of
641 human immunodeficiency virus. Retrovirology *15*, 41. 10.1186/s12977-018-0424-3.

642 28. Muranyi, W., Malkusch, S., Müller, B., Heilemann, M., and Kräusslich, H.-G. (2013). Super-
643 Resolution Microscopy Reveals Specific Recruitment of HIV-1 Envelope Proteins to Viral
644 Assembly Sites Dependent on the Envelope C-Terminal Tail. PLOS Pathogens *9*, e1003198.
645 10.1371/journal.ppat.1003198.

646 29. Laine, R.F., Goodfellow, G., Young, L.J., Travers, J., Carroll, D., Dibben, O., Bright, H., and
647 Kaminski, C.F. (2018). Structured illumination microscopy combined with machine learning
648 enables the high throughput analysis and classification of virus structure. eLife *7*, e40183.
649 10.7554/eLife.40183.

650 30. McMahon, A., Andrews, R., Groves, D., Ghani, S.V., Cordes, T., Kapanidis, A.N., and Robb,
651 N.C. (2023). High-throughput super-resolution analysis of influenza virus pleomorphism
652 reveals insights into viral spatial organization. PLOS Pathogens *19*, e1011484.
653 10.1371/journal.ppat.1011484.

654 31. Chen, Y.-C., Sood, C., Marin, M., Aaron, J., Gratton, E., Salaita, K., and Melikyan, G.B.
655 (2020). Super-Resolution Fluorescence Imaging Reveals That Serine Incorporator Protein 5
656 Inhibits Human Immunodeficiency Virus Fusion by Disrupting Envelope Glycoprotein
657 Clusters. ACS Nano *14*, 10929–10943. 10.1021/acsnano.0c02699.

32. Kovtun, O., Dickson, V.K., Kelly, B.T., Owen, D.J., and Briggs, J.A.G. (2020). Architecture of the AP2/clathrin coat on the membranes of clathrin-coated vesicles. Sci Adv *6*, eaba8381. 10.1126/sciadv.aba8381.

33. Wang, Y.E., Park, A., Lake, M., Pentecost, M., Torres, B., Yun, T.E., Wolf, M.C., Holbrook, M.R., Freiberg, A.N., and Lee, B. (2010). Ubiquitin-Regulated Nuclear-Cytoplasmic Trafficking of the Nipah Virus Matrix Protein Is Important for Viral Budding. PLOS Pathogens *6*, e1001186. 10.1371/journal.ppat.1001186.